

Burial-related Compaction Modifies Intrusion-induced Forced Folds: Implications for Reconciling Roof Uplift Mechanisms using Seismic Reflection Data

Craig Magee^{1,2*}, Murray Hoggett³, Christopher A-L Jackson¹, Stephen M. Jones³

¹Basins Research Group (BRG), Department of Earth Science and Engineering, Imperial College London, London, SW7 2BP

²School of Earth and Environment, University of Leeds, Leeds, LS2 9JT, UK

³School of Geography, Earth and Environmental Science, University of Birmingham, Birmingham, B15 2TT, UK

*corresponding author (c.magee@leeds.ac.uk)

Abstract

Space for shallow-level sills and laccoliths is commonly generated by bending and uplift of overlying rock and sediment. This so-called ‘roof uplift’ produces forced folds, the shape and amplitude of which reflect the geometry of underlying intrusions. The surface expression of forced folds can therefore be inverted to constrain intruding magma body properties, whilst ancient forced folds provide a record of sill and laccolith emplacement. Deciphering how shallow-level intrusion translates into roof uplift is thus critical to enhancing our understanding and forecasting of magma emplacement. To-date, emplacement models and surface deformation inversions are underpinned by the consideration that roof uplift is, to a first-order, an elastic process. However, several studies have suggested inelastic processes can accommodate significant magma volumes, implying first-order roof uplift may be a function of elastic *and* inelastic deformation. In particular, seismic reflection images of forced folds above ancient sills and laccoliths indicate final fold amplitudes can be substantially less (by up to 85%) than the underlying intrusion thickness. Although these seismic-based observations imply elastic and inelastic deformation accommodated intrusion, these studies do not consider whether burial-related compaction has reduced the original fold amplitude. Here, we use geological (e.g. lithology) and geophysical (e.g. seismic velocity) information from the Resolution-1 borehole offshore eastern New Zealand, which intersects a forced fold and upper ~50 m of a sill imaged in 2D seismic reflection data, to decompact the folded sequence and recover its original geometry. We show the Resolution Sill is likely ~117–187 m thick, depending on the interval velocity for the entire intrusion, whereas the forced fold has an apparent maximum amplitude of ~127 m, corresponding to a sill thickness-fold amplitude discrepancy of up to 32%. Decompaction indicates the original maximum forced fold amplitude likely ranged from ~131–185 m, suggesting post-emplacement, burial-related compaction of this and other forced folds may be the source of apparent discrepancies between fold amplitude and intrusion thickness. Whilst seismic reflection data can provide fundamental insights into how shallow-level emplacement translates into roof uplift and ground displacement, we show decompaction and backstripping are required to recover the original fold geometry.

Keywords: Forced fold; Sill; Seismic reflection; Emplacement; Roof uplift; Compaction

1. Introduction

Generating space to accommodate magma emplacement requires deformation of the host rock. Field- and seismic reflection-based studies of ancient intrusions, supported by various physical, numerical, and analytical modelling approaches, reveal sills and laccoliths emplaced at shallow-levels within the upper crust can be accommodated by elastic bending of the overburden and, potentially, the free surface (so-called ‘roof uplift’; e.g. Gilbert, 1877;

51 Johnson & Pollard, 1973; Pollard & Johnson, 1973; Koch et al. 1981; Fialko et al. 2001;
52 Smallwood & Maresh, 2002; Trude et al. 2003; Hansen & Cartwright, 2006; Bunger &
53 Cruden, 2011; Galland, 2012; Galland & Scheibert, 2013; Jackson et al. 2013; Magee et al.
54 2013a; van Wyk de Vries et al. 2014; Montanari et al. 2017; Reeves et al. 2018). Geodetic
55 data also suggest that short-timescale ground displacements at active volcanoes, generated by
56 sill or laccolith emplacement, reflect elastic deformation (e.g. Pagli et al. 2012; Castro et al.
57 2016; Ebmeier et al. 2018). These zones of roof uplift mimic the plan-view geometry of
58 underlying intrusion(s) and can thus be described as a form of ‘forced fold’ (e.g. Hansen &
59 Cartwright, 2006; Magee et al. 2013a); i.e. a fold with a morphology controlled by that of a
60 forcing member below (Stearns, 1978). By assuming purely elastic deformation
61 accommodates magma emplacement at shallow-levels, particularly when the intrusion
62 diameter (D) to emplacement depth (d) ratio is $\gg 4$, we can expect the original intrusion
63 thickness ($T_{0\max}$) to broadly equal the original amplitude ($F_{0\max}$) of the overlying forced fold
64 (i.e. $F_{0\max}/T_{0\max} = 1$) (Pollard & Johnson, 1973; Fialko et al. 2001; Hansen & Cartwright,
65 2006; Jackson et al. 2013).

66
67 Seismic reflection data reveal the current maximum amplitude (F_{\max}) of buried forced folds
68 can be up to 85% less than the measured maximum thickness (T_{\max}) of underlying,
69 crystallised sills or laccoliths (i.e. $F_{\max}/T_{\max} < 1$; Fig. 1A) (Hansen & Cartwright, 2006;
70 Jackson et al. 2013; Magee et al. 2013a). Such discrepancies between fold amplitude and
71 intrusion thickness, particularly where $F_{\max}/T_{\max} \ll 1$, have been suggested to relate to the
72 accommodation of magma by both elastic *and* inelastic deformation (Jackson et al. 2013;
73 Magee et al. 2013a; Magee et al. 2017). Syn-intrusion, fracture-driven porosity reduction,
74 faulting, and fluidisation of the host rock around exposed sills confirms that inelastic
75 deformation can partly and, perhaps in some instances, fully accommodate magma
76 emplacement (Figs 1B and C) (e.g. Johnson & Pollard, 1973; Morgan et al. 2008; Schofield
77 et al. 2012; Jackson et al. 2013; Schofield et al. 2014; Spacapan et al. 2016). It has also been
78 suggested that inelastic ductile strain and vertical compaction of deforming strata can cause
79 fold amplitudes to decay upwards, particularly if D/d is < 4 (Hansen & Cartwright, 2006;
80 Jackson et al. 2013). Seismic and field data therefore provide evidence for the
81 accommodation of magma by elastic *and* inelastic deformation, challenging the assumption
82 that emplacement models need only account for elastic processes (e.g. Magee et al. 2013a;
83 Galland & Scheibert, 2013; Holohan et al. 2015; Scheibert et al. 2017).

84
85 Seismic reflection data capture the current, and not necessarily the original, geometry of
86 ancient intrusions and forced folds. For example, original fold amplitudes and sill
87 thicknesses, and the ratio between them, may be modified post-emplacement by the: (i)
88 migration of magma away from the seismically resolved intrusion ($T_{\max} < T_{0\max}$) coupled with
89 little or no fold subsidence ($F_{\max} > T_{\max}$) (e.g. Reeves et al. 2018); (ii) deflation of the sill in
90 response to crystallisation of and/or volatile release from the magma ($T_{\max} < T_{0\max}$; e.g.
91 Caricchi et al. 2014), which could promote disproportionate fold subsidence ($F_{\max} > T_{\max}$); (iii)
92 erosion of the fold crest ($F_{\max} < T_{\max}$) (Hansen & Cartwright, 2006; Jackson et al. 2013);
93 and/or (iv) burial and compaction of the folded sequence ($F_{\max} < T_{\max}$) (Jackson et al. 2013).
94 No study has yet quantified how post-emplacement, burial-related compaction can modify
95 forced fold geometries and amplitudes. Without incorporating an assessment of how burial-
96 related compaction has affected the seismically resolved forced fold geometry and amplitude,
97 the role of inelastic processes in accommodating magma cannot be determined from seismic
98 reflection data alone.

99 Here, we examine a saucer-shaped sill, the Resolution Sill, and overlying forced fold imaged
100 in 2D seismic reflection data from the Canterbury Basin, offshore eastern New Zealand and
101 intersected by the Resolution-1 borehole (Fig. 2). The borehole penetrates the upper ~50 m of
102 the saucer-shaped sill, which can broadly be categorised as an olivine gabbro. Velocity
103 information from Resolution-1 facilitates depth conversion and decompaction of the seismic
104 reflection data; this allows us to constrain the original maximum fold amplitude (i.e. $F0_{max}$).
105 We show that burial-related compaction modifies ancient intrusion-induced forced folds
106 within sedimentary basins, reducing discrepancies between fold amplitude and sill thickness.
107 Before using seismic-based examples of ancient intrusion and forced fold pairs to postulate
108 emplacement mechanics at active volcanoes, it is essential to first account for burial-related
109 compaction.

110

111 **2. Geological setting**

112 The Canterbury Basin spans onshore and offshore SE New Zealand and formed during Late
113 Albian-to-Early Campanian rifting between New Zealand, Antarctica, and Australia (Fig. 2)
114 (Fulthorpe et al. 1996; Lu & Fulthorpe, 2004). The basement typically corresponds to
115 greywacke and argillite meta-sedimentary rocks of the Torlesse Supergroup (Permian-to-
116 Early Cretaceous; Fig. 3) (Uruski, 2010). In the north of the basin, within the study area, syn-
117 rift sedimentary strata deposited within graben and half-graben are dominated by the paralic
118 coal measures of the Broken River Formation, and marine siltstones and mudstones of the
119 Conway Formation (Fig. 3) (Carter, 1988; Killops et al. 1997; Schiøler et al. 2011). Onset of
120 post-rift, thermal subsidence in the Maastrichtian led to the deposition of the high-energy
121 marine Charteris Bay Sandstone (Lower Paleocene), which is overlain by tuffs of the View
122 Hill Volcanics, mudstones of the Conway Formation, and calcareous marine mudstones of
123 the Ashley Formation (Fig. 3) (Carter, 1988; Killops et al. 1997; Schiøler et al. 2011).
124 Micritic limestones attributed to the Amuri Formation were deposited between the Early
125 Oligocene and Early Miocene, although the majority of this time period corresponded to the
126 development of a regional unconformity across much of the Canterbury Basin (Fig. 3)
127 (Carter, 1988; Killops et al. 1997; Schiøler et al. 2011). Uplift along the Alpine Fault, and an
128 associated increase in the supply of terrigenous silt and sand, resulted in the deposition of the
129 marine Tokama Siltstone, which locally contains tuffs belonging to the Harper Hills Basalt
130 (K-Ar ages of 13.5 ± 0.4 – 11.0 ± 0.3 Ma), and overlying Kowai Formation (Early Miocene-to-
131 Recent; Fig. 3) (Sewell & Gibson, 1988; Lu et al. 2005).

132

133 Several discrete phases of intra-plate, post-Cretaceous magmatism and volcanism have been
134 recorded in the Canterbury Basin, including the View Hill Volcanics and the Harper Hills
135 Basalt (Fig. 3) (e.g. Timm et al. 2010; Reeves et al. 2018). It has been suggested that
136 volcanism occurred in response to decompression melting of upwelling heterogeneous
137 asthenospheric mantle following localised removal of gravitationally unstable lithospheric
138 material (Timm et al. 2010).

139

140 **3. Dataset**

141

142 **3.1 Borehole data**

143 Resolution-1 is located ~50 km south of Christchurch (Fig. 2) and was drilled in 1975 for
144 Shell BP Todd Canterbury Services Ltd (Milne, 1975). The borehole was drilled in a water
145 depth of 64 m and extends to a total depth of 1963.05 m, intersecting the Resolution Sill
146 between 1911.5–1963.05 m (Milne, 1975). Data available for the borehole include (Milne,
147 1975): (i) a well completion report containing petrological descriptions of cuttings and
148 sidewall core, sampled every 5 m between 1910–1958 m, and continuous core collected

149 between 1958.2–1963.05 m within the sill; (ii) sonic (ΔT), gamma ray (GR), calliper (CAL),
150 and spontaneous potential (SP) logs (Fig. 4); (iii) a petrophysical summary log plot; (iv) well
151 formation tops, ages, and lithological descriptions; and (v) K-Ar ages of 12 ± 2 Ma for the sill.
152 Density logs, neutron porosity logs, thin sections, or photomicrographs are not available to
153 corroborate the petrographic descriptions.

154

155 Resolution-1 has sparse time-depth information. To facilitate depth-conversion of the seismic
156 reflection data, we therefore derived a time-depth curve by integrating sonic log data after
157 using a median filter with a window of five samples to remove spikes caused by sample
158 skipping (Fig. 4). The sonic log data were also used to calculate a compressional wave (V_p)
159 velocity log by taking the reciprocal of the interval transit time log and converting from feet
160 to metres, and to define average interval velocities for different units (Fig. 4). For example,
161 the average interval velocity within the Resolution Sill intersected by the borehole is 5.2 km s^{-1}
162 (Fig. 4), with a standard deviation of 0.3 km s^{-1} . Although the average interval velocity of
163 the sill where it is intersected by Resolution-1 can be defined (i.e. 5.2 km s^{-1}), the borehole
164 does not extend through the entire intrusive body; as a result, we model a range of sill
165 velocities ($4.5\text{--}6.0 \text{ km s}^{-1}$) to estimate possible intrusion thicknesses (Smallwood & Maresh,
166 2002). Velocity data in the water column and the shallowest sedimentary strata were not
167 recorded, so we assume values of 1.5 km s^{-1} between 0–64 m (i.e. seawater) and 1.8 km s^{-1}
168 between 64–385 m (i.e. near-seabed sediments) (Fig. 4).

169

170 **3.1.1 Petrological description of the Resolution Sill**

171 The petrological description of the Resolution Sill was provided by Dr G. A. Challis of the
172 New Zealand Geological Survey (Milne, 1975). Based on 5 m-spaced cuttings collected
173 between 1911.5–1958 m, the Resolution Sill is best described as a medium-to-coarse grained
174 quartz gabbro comprising plagioclase, quartz, titanite, and aegirine. Minor amounts of
175 magnetite, ilmenite, and biotite also occur. Some fine-grained, glassy, black rock chips,
176 which contain white spherules, originate from the top contact chilled margin (see below).

177

178 At the top of the continuous core collected from the Resolution Sill, which corresponds to a
179 depth of 1958.2 m, the intrusion is a coarse-grained quartz syenogabbro primarily comprising
180 titanite rimmed by aegirine augite, zoned plagioclase (labradorite to oligoclase) rimmed
181 by anorthoclase, and ilmenite; fine-grained, quartz, biotite, apatite, and chlorite also occur
182 (Table 1). Below 1958.3 m, quartz is absent and the Resolution Sill can be broadly classified
183 as a teschenite that consists of plagioclase, titanite, analcite, anorthoclase, and
184 occasionally olivine with accessory apatite, ilmenite, magnetite, and zeolites (Table 1).

185 Variations in the abundance of olivine and titanite between ~1958–1963 m indicate the
186 Resolution Sill is subtly layered (Table 1).

187

188 Petrological analyses of cuttings reveal that a 44 m thick (from 1877.5–1911.5 m)
189 sedimentary succession directly overlying the sill is heavily pyritised and contains abundant
190 zeolites; this is particularly marked in the first 25 m above the sill. These mineral phases may
191 have formed in response to contact metamorphism and, thereby, potentially define the
192 thermal aureole of the Resolution Sill (Fig. 4).

193

194 **3.2 Seismic reflection data**

195 This study utilizes three, zero-phase, time-migrated, 2D seismic reflection surveys (the ANZ,
196 CB82, and Sight surveys; Fig. 2). We focus on an area that covers $\sim 3000 \text{ km}^2$ and has a total
197 seismic line length of $\sim 484 \text{ km}$ (Fig. 2). Line spacing for the different vintage seismic data
198 ranges from 3.5–16 km (Fig. 2B). Seismic data are displayed with a zero-phase SEG normal

199 polarity; a downward increase in acoustic impedance correlates to a positive (black/red)
200 reflection, whilst a negative (white/blue) reflection corresponds to a downward decrease in
201 acoustic impedance (Fig. 5). Interval velocities derived from borehole data were used to
202 convert the seismic reflection data from depth in seconds two-way time (TWT) to depth in
203 metres (Figs 4 and 5). We only depth-converted data above Top Basement because the
204 lithology and physical properties (e.g. V_p) of the underlying Torlesse Supergroup are
205 unknown (Fig. 5C).

206

207 **3.2.1 Data resolution**

208 The resolution of a studied interval in seismic reflection data is dependent on the dominant
209 wavelength (λ) of the seismic waves, with $\lambda = v/f$, where v is the interval velocity and f is the
210 dominant frequency (Brown, 2004). In order to distinguish reflections emanating from two
211 distinct boundaries (e.g. the top and base of a sill), their vertical distance needs to exceed the
212 limit of separability ($\sim\lambda/4$) for the data (Brown, 2004). If the vertical distance between the
213 boundaries is less than the limit of separability, the two reflections will interfere on their
214 return to the surface and cannot be deconvolved; they will appear as tuned reflection
215 packages, the true thickness of which cannot be determined (Brown, 2004). The limit of
216 visibility ($\sim\lambda/30$) defines the minimum vertical distance between two boundaries required to
217 produce a tuned reflection package that can be distinguished from noise in the seismic
218 reflection data (Brown, 2004). Interval velocities of 2.2–3.2 km s⁻¹ for the sedimentary
219 sequence in the section of interest (Fig. 4), coupled with a seismic dominant frequency that
220 decreases with depth from ~40 to 25 Hz, suggests that the limits of separability and visibility
221 for the data decrease with depth from ~32 to 14 m and ~4 to 2 m, respectively. Assuming the
222 entire Resolution Sill has an interval of velocity of 5.2 km s⁻¹, equal to that of the upper 50 m
223 intersected by Resolution-1, a surrounding dominant frequency of ~25 Hz indicates its limits
224 of separability and visibility are ~52 m and ~7 m, respectively. However, if we consider that
225 the average interval velocity of the Resolution Sill is more variable (i.e. 4.5–6.0 km s⁻¹), the
226 maximum limits of separability and visibility may be ~60 m and ~6 m, respectively.
227 Reflections from the top and base of the Resolution Sill where it is >60 m thick will therefore
228 be distinguishable in the seismic data, whereas parts of the sill <60 m thick but over >6 m
229 thick will be expressed as tuned reflection packages (see Smallwood & Maresh, 2002; Magee
230 et al. 2015; Eide et al. 2017). Where the Resolution Sill is <7 m thick, it is unlikely to be
231 detectable in the seismic reflection data.

232

233 **3.2.2 Seismic Interpretation**

234 The study area contains several high-amplitude reflections that are laterally discontinuous
235 and can typically be sub-divided into a strata-concordant inner region surrounded by a
236 transgressive, inward-dipping limb; i.e. they display a saucer-shaped morphology (Fig. 5).
237 We mapped these reflections and interpret them as sills because: (i) one corresponds to the
238 Resolution Sill intersected by the Resolution-1 borehole (Fig. 5); and (ii) they are
239 geometrically similar to igneous saucer-shaped sills observed in the field and imaged in other
240 seismic reflection datasets (e.g. Thomson & Hutton, 2004; Planke et al. 2005; Polteau et al.
241 2008; Magee et al. 2016). For all sills we mapped the top contact (TS) and, where seismically
242 resolved, the base sill (BS) (Fig. 5). In addition to sills, we mapped nine key seismic horizons
243 and tied them to the Resolution-1 borehole (Figs 3, 4, and 5): TB = Top Basement (~84 Ma);
244 H1 = Intra-Conway Formation unconformity, above the View Hill volcanics (Mid-
245 Palaeocene, ~58 Ma); H2 = Intra-Ashley Formation unconformity (Mid-Eocene, ~45 Ma);
246 H3 = Top Omihi Formation (Early Oligocene, ~16 Ma); H4 = lowermost Intra-Tokama
247 Formation (Early to Mid-Miocene, ~14 Ma); H5 = Intra-Tokama Formation (Mid-Miocene,

248 ~14 Ma); H6 = Base Harper Hill Basalts (Mid-Miocene, $\sim 13.5 \pm 0.4$ Ma) and top of the force
249 folds; H7 = Top Tokama unconformity (Miocene to Pliocene, ~ 6 Ma); and H8 = seabed.

250

251 The limited resolution of the seismic reflection data means we cannot ascertain whether
252 erosion has modified the geometry of the fold top (i.e. H6) and reduced its amplitude post-
253 emplacement (e.g. Fig. 5C). We therefore measure amplitude along the prominent intra-fold
254 horizon H3 (e.g. Fig. 5C). To determine fold amplitude we measure the vertical distance
255 between the top of H3 and an inferred pre-fold datum constructed by extrapolating the
256 regional trend of H3 from areas where there are no sills or forced folds (Fig. 5C inset). The
257 maximum vertical distance between H3 and the pre-fold datum is the maximum fold
258 amplitude (F_{\max} ; Fig. 5C). Sill thickness is measured as the vertical distance between TS and
259 BS, with the maximum sill thickness defined by T_{\max} (Fig. 5C).

260

261 **3.3 Decompression and backstripping**

262 Whilst several studies suggest cases where $F_{\max}/T_{\max} \ll 1$ reflects magma accommodated by
263 elastic *and* inelastic deformation processes, they do not quantitatively evaluate the role of
264 burial and compaction in modifying forced fold geometry (Jackson et al. 2013; Magee et al.
265 2013a; Magee et al. 2017). Loading of sedimentary sequences during burial promotes
266 progressive loss of porosity with depth (i.e. compaction), and causes beds to become thinner
267 and structures (e.g. faults) to flatten. The compaction of strata at any given depth is controlled
268 by its lithology and lithostatic load. Because crystalline intrusive rocks have virtually no
269 porosity and can be considered incompressible T_{\max} will not change with burial. However,
270 compaction of the overlying sedimentary sequence is expected to reduce F_{\max} and therefore
271 decrease of F_{\max}/T_{\max} . The sedimentary sequence adjacent to the sill is overlain by a thicker
272 column of sediment/rock, meaning it will compact more than where it is folded above the sill;
273 this variation in lithostatic load across the fold can promote differential compaction (Hansen
274 & Cartwright, 2006; Schmiedel et al. 2017). Evaluating the role of post-emplacement
275 compaction in modifying forced folds is critical to establishing the relationship between the
276 original maximum fold amplitude ($F_{0\max}$) and intrusion thickness, which can be used to
277 inform interpretation of emplacement mechanics. To extract $F_{0\max}$, we decompact and
278 backstrip the forced fold. Note we do not take into account processes that may alter sill
279 thickness (e.g. contraction during crystallisation; Caricchi et al. 2014) and thus assume
280 $T_{\max} = T_{0\max}$.

281

282 **3.3.1 Forward modelling**

283 Decompacting and backstripping sedimentary sequences imaged in depth-converted seismic
284 reflection data involves restoring the initial porosity (ϕ_0) of strata at the top of the sequence
285 from its current porosity (ϕ), by removing its overburden. This technique normally involves
286 estimating a porosity log from sonic log data using either the Wyllie time-average method or
287 Raymer-Hunt-Gardner empirical relationship (Wyllie et al. 1956; Raymer et al. 1980).
288 However, given the shallow depth of our interval of interest (i.e. 1–2 km) and the limited log
289 data available (e.g. there is no density log), we cannot reliably assess the accuracy of current
290 porosity logs derived from these methods. We therefore apply forward modelling techniques
291 to establish whether plausible decompacted and backstripped scenarios are realistic and how
292 they impact fold geometry. In particular, based on the lithological information from
293 Resolution-1, we model a series of different parameter ranges and combinations to assess
294 potential variations between sill thickness and the original fold amplitude. Because estimates
295 of ϕ_0 and the compaction length scale are not available, we model a range of realistic values
296 (Sclater and Christie, 1980): (i) ϕ_0 is considered to range from 0.7–0.25, consistent with a
297 range of siliciclastic sequences; and (ii) compaction length scale ranges from 3.7–1.4.

298

299 4. Observations

300

301 4.1 Resolution Sill

302

303 4.1.1 Resolution Sill well-log response

304 The Resolution Sill is characterised by an abrupt increase in V_p , from $\sim 3.0 \text{ km s}^{-1}$ in the
305 overlying strata to $\sim 5.2 \text{ km s}^{-1}$ within the sill (Fig. 4). Within the sill itself, values of V_p , GR,
306 and SP vary substantially on a metre to decametre-scale (Fig. 4).

307

308 4.1.2 Geometry

309 The Resolution Sill is observed on two seismic lines, with its top corresponding to a high-
310 amplitude, positive polarity reflection (TS; Figs 4 and 5). Where the base of the sill is
311 resolved, it is characterised by a discrete, moderate-to-high amplitude, negative polarity
312 reflection (BS) that appears to coincide with the top of the basement (TB) at a present day
313 depth of $\sim 2 \text{ km}$ (Fig. 5). Overall, the 54 km^2 sill has an elliptical, saucer-shaped morphology
314 with a NW-trending, long axis of $\sim 6.2 \text{ km}$ and a NE-trending short axis of $\sim 2.8 \text{ km}$ (Fig. 6).
315 The strata-concordant inner sill is sub-circular, with a diameter (D) of $\sim 2.2 \text{ km}$, passing
316 laterally into gently (8°), inward-dipping, up to $\sim 0.4 \text{ km}$ high transgressive limbs to the SE
317 and NW (Figs 5 and 6). Towards the south-eastern edge of the Resolution Sill, at its
318 shallowest level, the transgressive limb transitions into a strata-concordant outer rim (Figs 5
319 and 6).

320

321 Intrusion thickness appears variable across the strata-concordant inner sill, although there is a
322 first-order decrease away from the centre; assuming an interval velocity of 5.2 km s^{-1} for the
323 entire sill, its thickness ranges from $\sim 138 \text{ m}$ (T_{max}) to $\leq 52 \text{ m}$ (Figs 6C and 7). Superimposed
324 onto this outward-thinning trend within the inner sill are apparently several abrupt changes in
325 sill thickness (e.g. there is a $\sim 75 \text{ m}$ change at A-A'; Fig. 7). However, because the lower
326 portion of the sill is not intersected by Resolution-1, we do not know if it is characterised by
327 similar velocities. We also do not know whether the interval velocity of the sill varies
328 laterally. We therefore calculate sill thickness using a range of feasible interval velocities (i.e.
329 $4.5\text{--}6.0 \text{ km s}^{-1}$). The envelope calculated for this velocity range constrains how thickness may
330 vary along-strike when the sill velocity across (i.e. vertically and laterally) the intrusion is
331 constant (e.g. 4.5 or 5.2 km s^{-1}) or variable (e.g. if the velocity decreases towards its edges)
332 (Fig. 7). For a range of interval velocities, we show the sill: (i) could be up to $\sim 187 \text{ m}$ thick
333 (i.e. T_{max}); (ii) maintains a first-order decrease in thickness from its centre outwards; and (iii)
334 thickness still appears to show local, abrupt variations, although the magnitude of these
335 changes may be suppressed depending on how velocity varies laterally (Fig. 7). For example,
336 dependent on sills the velocity configuration, the thickness change at A-A' could be up to
337 $\sim 149 \text{ m}$, or down to $\sim 17 \text{ m}$. The outer portions of the transgressive sill limbs are defined by
338 tuned reflection packages, such that their vertical thickness cannot be measured; where tuning
339 occurs we consider intrusion thickness can range from $60\text{--}6 \text{ m}$ (i.e. the limits of separability
340 and visibility, respectively) (Figs 5 and 7).

341

342 The Resolution Sill is bordered to the SW, NW, and NE by three additional saucer-shaped
343 sills; the 3D geometry of these neighbouring sills cannot be constrained as they cannot be
344 mapped sufficiently on multiple seismic lines (Fig. 5). In cross-section, the sills to the SW
345 and NW display similar geometries and emplacement depths to the Resolution Sill, whereas
346 the base of the north-eastern sill broadly coincides with Horizon H1 (Fig. 5).

347

348 **4.2 Host rock structure**

349 Strata directly above the Resolution Sill, up to H6, are folded (Figs 5 and 8). The $\sim 58 \text{ km}^2$,
350 elliptical (i.e. $\sim 6.2 \text{ km} \times 3 \text{ km}$) dome is relatively flat-topped, with uplift primarily
351 accommodated by monoclinical bending directly above the transgressive limbs of the
352 Resolution Sill, which cross-cut the lowermost folded strata (Figs 5 and 8). The top of the
353 fold corresponds to H6, i.e. the $\sim 12.5 \text{ Myr}$ old base of the 9 m thick Harper Hills Basalt, and
354 is overlapped by overlying, sub-horizontal strata of the Tokama Siltstone (Figs 3 and 5). Whilst
355 these seismic-stratigraphic onlap relationships indicate H6 represented the syn-intrusion free
356 surface, the limited resolution of the seismic reflection data means we cannot ascertain
357 whether erosion has subtly modified the geometry of the fold crest. The maximum fold
358 amplitude (F_{max}) at H3 is $\sim 127 \text{ m}$, with amplitude gradually and smoothly decreasing towards
359 the fold periphery (Fig. 7). The vertical distance between H6 and TS is $\sim 0.75 \text{ km}$ (Fig. 5C).

360

361 Similar folds are developed above the three sills neighbouring the Resolution Sill; the top of
362 these folds all occur at H6 and their boundaries directly overlie lateral sill tips (Figs 5 and
363 8). The supra-sill fold to the SW of the Resolution Sill is associated with several mound-like
364 structures marked by moderate-amplitude, positive polarity (black) reflections that downlap
365 onto Horizon H6 and themselves are overlapped H6–H7 strata (Fig. 5A). These mounds are up
366 to $\sim 315 \text{ ms}$ TWT high (their height in metres cannot be calculated without knowledge of their
367 V_p) and have diameters up to $\sim 3.5 \text{ km}$. The mounds appear to have erosional bases that
368 truncate underlying strata, including H6 (Fig. 5A). Internal reflections within the mounds are
369 relatively poorly imaged but appear to have a convex-upwards morphology (Fig. 5A).

370

371 **4.3 Fold amplitude compared to sill thickness**

372 The maximum sill thickness (T_{max}) is estimated to be $\sim 138 \text{ m}$, but may range from ~ 117 – 187
373 m thick depending on the interval velocity of the entire sill (Fig. 7). The maximum fold
374 amplitude (F_{max}) measured at H3 is $\sim 127 \text{ m}$ (Fig. 7). Comparing these intrusion and fold
375 measurements suggests $F_{\text{max}}/T_{\text{max}}$ is ~ 0.92 , potentially ranging from ~ 0.68 – 1.09 . We also note
376 there is a lateral offset of $\sim 400 \text{ m}$ between the locations of F_{max} and T_{max} (Fig. 7). Fold
377 amplitude and sill thickness both display a first-order decrease towards their peripheries,
378 although sill thickness does appear to vary abruptly in places where fold amplitude does not
379 (Fig. 7). It is difficult to determine how fold amplitude relates to the thickness of the
380 transgressive limbs because the latter are only expressed as tuned reflection packages so only
381 their maximum (i.e. the limit of separability, 52 m) and minimum (i.e. the limit of visibility, 7
382 m) thicknesses can be constrained (Figs 5 and 7).

383

384 **4.3.1 Decompaction and backstripping results**

385 Decompaction of the amplitude profile across the top of the fold intersected by Resolution-1
386 reveals that its shape is maintained but its maximum amplitude increases from $\sim 127 \text{ m}$ (i.e.
387 F_{max}) to up to ~ 131 – 185 m (i.e. $F_{0\text{max}}$; Fig. 9). Uncertainties in the decompaction input
388 parameters means the original fold amplitude profile cannot be absolutely determined.
389 Although calculated $F_{0\text{max}}/T_{\text{max}}$ values range from 0.70 – 1.58 , the breadth of which is a
390 function of the broader range of possible scenarios compared to $F_{\text{max}}/T_{\text{max}}$, it is clear there is a
391 greater overlap between likely sill thicknesses and amplitude values after decompaction (Fig.
392 9). Following decompaction, the vertical distance between H6 and TS (i.e. the emplacement
393 depth) is $\sim 0.8 \text{ km}$.

394

395 **5. Discussion**

396

397 **5.1 Timing of sill emplacement and forced folding**

398 The top of the forced fold overlying the Resolution Sill corresponds to Horizon H6, where a
399 thin tuff, which is genetically related to the Harper Hills Basalt, is interbedded with the
400 Tokama Siltstone (Fig. 5). Onlap of the marine, middle-to-late Miocene Tokama Siltstone
401 onto Horizon H6 suggest it formed the palaeoseabed during sill emplacement and forced
402 folding. Where exposed onshore, the tholeiitic Harper Hills Basalts have K-Ar ages ranging
403 from 13.5 ± 0.4 – 11.5 ± 0.3 Ma (Sewell & Gibson, 1988), which can be used as a proxy for the
404 age of H6. This potential age range for H6 overlaps with the radiometric date obtained for the
405 Resolution Sill (i.e. 12 ± 2 Ma; Milne, 1975), suggesting sill emplacement and forced folding
406 occurred ~ 12 Ma.

407

408 Sills and forced folds adjacent to the Resolution Sill display similar seismic-stratigraphic
409 relationships (i.e. H6 marks the fold tops) and, in places, are overlain by mound-like features
410 we interpret as volcanoes based on: (i) their moderate-to-high amplitude, positive polarity top
411 contacts indicative of a downward increase in seismic velocity and density, consistent with a
412 transition from sedimentary to igneous rocks (e.g. Symonds et al. 1998; Planke et al. 2005);
413 (ii) observed truncation underlying strata, similar to eye-shaped hydrothermal vents,
414 suggesting they formed via explosive activity (e.g. Jamtviet et al. 2004; Hansen, 2004; Planke
415 et al. 2005; Magee et al. 2016b); and (iii) they have similar geometries and internal
416 architectures to volcanic vents and volcanoes observed in other sedimentary basins (e.g.
417 Symonds et al. 1998; Jackson, 2012; Magee et al. 2013b). Overall, our seismic-stratigraphic
418 observations, coupled with radiometric dating of the Resolution Sill and the Harper Hills
419 Basalt onshore, indicate a phase of magmatism and volcanic activity across the northern
420 Canterbury Basin during the Mid-Miocene (Sewell & Gibson, 1988; Timm et al. 2010).

421

422 **5.2 Emplacement mechanics and burial-related compaction**

423 For shallow-level sills and laccoliths accommodated purely by elastic bending of the
424 overburden, we may expect the original fold amplitude, measured at the fold top, and sill
425 thickness to be broadly equal (i.e. $F_{0\max}/T_{0\max} = 1$) (e.g. Pollard & Johnson, 1973; Fialko et al.
426 2001; Hansen & Cartwright, 2006; Jackson et al. 2013). The ratio between the original fold
427 amplitude and sill thickness is partially controlled by the ratio of the inner sill diameter (D)
428 and depth of emplacement (d), with larger sills intruded at shallower depths capable of
429 generating more bending, and thus uplift of the contemporaneous free surface, than a smaller
430 sill at greater depths (e.g. Pollard & Johnson, 1973; Fialko et al. 2001; Hansen & Cartwright,
431 2006; Jackson et al. 2013). In particular, if the D/d ratio is >4 , it is considered that the
432 overburden will not resist bending and elastic deformation will therefore fully accommodate
433 magma emplacement (Pollard & Johnson, 1973; Hansen & Cartwright, 2006). Decompaction
434 of our data indicates the Resolution Sill, which has an inner sill diameter (D) of ~ 2.2 km, was
435 emplaced at a depth (d) of ~ 0.8 km beneath the contemporaneous surface (i.e. H6) and thus
436 had a D/d ratio of ~ 2.75 . Given a D/d ratio <4 , the model of Pollard & Johnson (1973)
437 suggests that the overburden may have resisted bending and, in addition to elastic
438 deformation, promoted inelastic vertical compaction or ductile strain, thereby suppressing
439 forced fold amplitude (i.e. $F_{0\max} < T_{0\max}$) (see also Hansen & Cartwright, 2006; Jackson et al.
440 2013).

441

442 In contrast to previous studies, we quantitatively assess the impact post-emplacement
443 compaction during burial has on fold geometry (principally amplitude) and, therefore,
444 $F_{0\max}/T_{\max}$ as opposed to F_{\max}/T_{\max} (cf. Hansen & Cartwright, 2006; Jackson et al. 2013;
445 Magee et al. 2013a; Magee et al. 2017). We show that following decompaction and
446 backstripping, the overall fold geometry is maintained but its amplitude increases from 127 m
447 (F_{\max}) up to 131–185 m ($F_{0\max}$) (Fig. 9). These potential $F_{0\max}$ values, coupled with a sill

448 thickness of 117–187 m, means $F_{0\max}/T_{\max}$ ranges from 0.70–1.58; this is greater than our
449 measured F_{\max}/T_{\max} range (i.e. 0.81–1.00), which we attribute to the broader range of
450 scenarios we test in calculating $F_{0\max}/T_{\max}$. Considering uncertainties in the various
451 parameters controlling $F_{0\max}/T_{\max}$ measurement (e.g. sill and strata interval velocities,
452 incorrect extrapolation of the pre-fold datum), our calculated $F_{0\max}/T_{\max}$ range of 0.70–1.58
453 suggests: (i) fold amplitude and sill thickness could be equal; (ii) fold amplitude may be less
454 than sill thickness by up to 30%, a scenario consistent with a D/d ratio of ~ 2.75 ; or (iii) fold
455 amplitude is greater than sill thickness by up to $\sim 58\%$, which could occur when thin (i.e. with
456 thicknesses below the limit of visibility) sills that contributed to uplift are not seismically
457 resolved (Reeves et al. 2018). Although uncertainties mean we cannot ascertain the true,
458 original sill-fold relationships, there qualitatively appears to be a better fit between the
459 potential ranges of sill thickness and decompacted fold amplitude (Fig. 9).

460

461 In addition to burial-related compaction, it is also worth highlighting that F_{\max}/T_{\max}
462 discrepancies could be attributed to (Hansen & Cartwright, 2006; Jackson et al. 2013; Magee
463 et al. 2013a): (i) reduction of fold amplitude due to erosion of the fold crest; (ii) incorrect
464 depth conversion; (iii) strain interference with adjacent folds during deformation; (iv) out-of-
465 plane deformation; or (v) changes in intrusion geometry. We measure amplitude from an
466 intra-fold horizon (i.e. H3), so discount erosion of the fold crest as a mechanism for reducing
467 F_{\max} and producing F_{\max}/T_{\max} ratios <1 (e.g. 0.81) (Fig. 5C). By using velocity data from
468 Resolution-1 and calculating sill thickness for a range of velocity values means we have
469 better control on depth conversion parameters than previous studies, yet our results highlight
470 F_{\max}/T_{\max} discrepancies <1 are still plausible (cf. Hansen & Cartwright, 2006; Jackson et al.
471 2013; Magee et al. 2013a; Magee et al. 2017). The Resolution Sill and overlying forced fold
472 are adjacent to and abut sill-fold pairs, of the same age, to the NW and SW (Figs 5 and 8),
473 implying strain interference between the folds may have enhanced or inhibited fold growth;
474 we cannot quantify whether strain interference had a positive or negative impact on F_{\max} .
475 Abrupt, localised variations in thickness across the sill are not reflected by the overlying fold
476 shape (Figs 5, 7, and 9); this local decoupling between sill and fold shape may suggest
477 vertical displacement induced by sill intrusion is distributed across an area because the
478 overburden has some flexural strength (see Stearns, 1978). The fold profile we measure thus
479 does not capture and may have been modified by localised out-of-plane deformation or
480 changes in intrusion geometry; these observations imply that relatively simple ground
481 deformation patterns may be generated by intrusions with complex geometries. Whether
482 folded strata respond (i.e. deform) to small-scale changes in intrusion thickness is a function
483 of emplacement depth and various host rock properties (e.g. flexural rigidity, bed thickness,
484 co-efficient of friction between layers) (e.g. Stearns, 1978).

485

486 Overall, our work implies that explicitly accounting for burial-related compaction likely
487 reduces measured F_{\max}/T_{\max} discrepancies (cf. Jackson et al. 2013; Magee et al. 2013a). We
488 show that emplacement of the Resolution Sill was principally accommodated by elastic
489 bending of the overburden, but cannot confirm whether inelastic deformation also generated
490 space for the intrusion. Further work is required to test the impact of burial-related
491 compaction on the geometry and amplitude of seismically imaged forced folds.

492

493 **6. Conclusions**

494 Elastic bending and uplift of overlying rock and sediment, and potentially the free surface,
495 can accommodate emplacement of shallow-level, tabular intrusions; this intrusion-induced
496 deformation is a form of ‘forced folding’. Many numerical and analytical models examining
497 sill and laccolith emplacement, as well as inversions of ground displacement data at active

498 volcanoes used to recover information pertaining to subsurface magma movement, typically
499 only incorporate elastic processes and neglect inelastic deformation mechanisms. Whilst the
500 assumption that host rock deformation is purely elastic can be applied to many scenarios,
501 several seismic reflection-based studies have suggested that synchronous elastic *and* inelastic
502 processes can generate space for magma intrusion. This interpretation that elastic and
503 inelastic processes can accommodate magma, which is supported by some outcrop data and
504 analytical modelling, is based on some seismically imaged forced folds having amplitudes
505 much smaller than the thickness of the underlying intrusion; i.e. elastic bending is expected to
506 produce folds with amplitudes broadly equal to the thickness of the underlying intrusion.
507 However, these seismic-based studies do not quantitatively account for post-emplacement,
508 burial-related compaction of forced folds, which may be expected to reduce their amplitude.
509 Through analysis of the Resolution Sill and its overlying forced fold, imaged in seismic
510 reflection data offshore eastern New Zealand and intersected by the Resolution-1 borehole,
511 we present the first robust decompaction and backstripping of an intrusion-induced forced
512 fold to constrain its original geometry. Our results highlight the forced fold had an original
513 amplitude of ~131–185 m, but burial-related compaction has reduced its amplitude to ~127
514 m. The top and base of the Resolution Sill are seismically distinguishable across its centre,
515 where it has a maximum thickness of 117–187 m, depending on the interval velocity of the
516 entire sill. Although uncertainties still exist, we show that decompaction reduces and
517 potentially fully accounts for apparent discrepancies between fold amplitudes and sill
518 thicknesses. Our observations also suggest relatively simple fold shapes may be produced by
519 complex intrusion geometries, involving local abrupt changes in thickness. Seismic reflection
520 data provides unprecedented insights into the 3D geometry of natural intrusions and forced
521 folds, but we highlight the need to consider the role of burial-related compaction in
522 modifying fold shapes and amplitudes.

523

524 **7. Acknowledgements**

525 CM acknowledges funding from an Imperial College Junior Research Fellowship and a
526 NERC Independent Research Fellowship (NE/R014086/1). MH acknowledges funding from
527 NERC studentship NE/1369185. New Zealand Petroleum and Minerals are thanked for
528 providing all data used (i.e. 2D seismic reflection lines, borehole data, and relevant reports),
529 which are freely available through <https://www.nzpam.govt.nz/>. Schlumberger are thanked
530 for provision of Petrel seismic interpretation software.

531

532 **8. References**

533 Brown, A.R., 2011. *Interpretation of three-dimensional seismic data*. Society of Exploration
534 Geophysicists and American Association of Petroleum Geologists.
535 Bungler, A.P. and Cruden, A.R., 2011. Modeling the growth of laccoliths and large mafic
536 sills: Role of magma body forces. *Journal of Geophysical Research: Solid Earth*, 116(B2).
537 Caricchi, L., Biggs, J., Annen, C. and Ebmeier, S., 2014. The influence of cooling,
538 crystallisation and re-melting on the interpretation of geodetic signals in volcanic
539 systems. *Earth and Planetary Science Letters*, 388, pp.166-174.
540 Carter, R.M., 1988. Post-breakup stratigraphy of the Kaikoura Synthem (Cretaceous-
541 Cenozoic), continental margin, southeastern New Zealand. *New Zealand journal of geology
542 and geophysics*, 31(4), pp.405-429.
543 Castro, J.M., Cordonnier, B., Schipper, C.I., Tuffen, H., Baumann, T.S. and Feisel, Y., 2016.
544 Rapid laccolith intrusion driven by explosive volcanic eruption. *Nature communications*, 7,
545 p.13585.
546 Ebmeier, S.K., Andrews, B.J., Araya, M.C., Arnold, D.W.D., Biggs, J., Cooper, C., Cottrell,
547 E., Furtney, M., Hickey, J., Jay, J. and Lloyd, R., 2018. Synthesis of global satellite

548 observations of magmatic and volcanic deformation: implications for volcano monitoring &
549 the lateral extent of magmatic domains. *Journal of Applied Volcanology*, 7(1), p.2.

550 Eide, C.H., Schofield, N., Lecomte, I., Buckley, S.J. and Howell, J.A., 2018. Seismic
551 interpretation of sill complexes in sedimentary basins: implications for the sub-sill imaging
552 problem. *Journal of the Geological Society*, 175(2), pp.193-209.

553 Fialko, Y. and Simons, M., 2001. Evidence for on-going inflation of the Socorro magma
554 body, New Mexico, from Interferometric synthetic aperture radar imaging. *Geophysical
555 Research Letters*, 28(18), pp.3549-3552.

556 Fulthorpe, C.S., Carter, R.M., Miller, K.G. and Wilson, J., 1996. Marshall Paraconformity: a
557 mid-Oligocene record of inception of the Antarctic Circumpolar Current and coeval glacio-
558 eustatic lowstand?. *Marine and petroleum geology*, 13(1), pp.61-77.

559 Galland, O., 2012. Experimental modelling of ground deformation associated with shallow
560 magma intrusions. *Earth and Planetary Science Letters*, 317, pp.145-156.

561 Galland, O. and Scheibert, J., 2013. Analytical model of surface uplift above axisymmetric
562 flat-lying magma intrusions: Implications for sill emplacement and geodesy. *Journal of
563 Volcanology and Geothermal Research*, 253, pp.114-130.

564 Gilbert, G.K., 1877. *Report on the Geology of the Henry Mountains*. US Government
565 Printing Office.

566 Hansen, D.M., 2006. The morphology of intrusion-related vent structures and their
567 implications for constraining the timing of intrusive events along the NE Atlantic
568 margin. *Journal of the Geological Society*, 163(5), pp.789-800.

569 Hansen, D.M. and Cartwright, J., 2006. The three-dimensional geometry and growth of
570 forced folds above saucer-shaped igneous sills. *Journal of Structural Geology*, 28(8),
571 pp.1520-1535.

572 Holohan, E.P., Sudhaus, H., Walter, T.R., Schöpfer, M.P. and Walsh, J.J., 2017. Effects of
573 Host-rock Fracturing on Elastic-deformation Source Models of Volcano Deflation. *Scientific
574 Reports*, 7(1), p.10970.

575 Jackson, C.A.L., 2012. Seismic reflection imaging and controls on the preservation of ancient
576 sill-fed magmatic vents. *Journal of the Geological Society*, 169(5), pp.503-506.

577 Jackson, C.A., Schofield, N. and Golenkov, B., 2013. Geometry and controls on the
578 development of igneous sill-related forced folds: A 2-D seismic reflection case study from
579 offshore southern Australia. *Bulletin*, 125(11-12), pp.1874-1890.

580 Jamtveit, B., Svensen, H., Podladchikov, Y.Y. and Planke, S., 2004. Hydrothermal vent
581 complexes associated with sill intrusions in sedimentary basins. *Physical Geology of High-
582 Level Magmatic Systems. Geological Society, London, Special Publications*, 234, pp.233-241.

583 Johnson, A.M. and Pollard, D.D., 1973. Mechanics of growth of some laccolithic intrusions
584 in the Henry mountains, Utah, I: field observations, Gilbert's model, physical properties and
585 flow of the magma. *Tectonophysics*, 18(3-4), pp.261-309.

586 Killops, S.D., Cook, R.A., Sykes, R. and Boudou, J.P., 1997. Petroleum potential and oil-
587 source correlation in the Great South and Canterbury Basins. *New Zealand Journal of
588 Geology and Geophysics*, 40(4), pp.405-423.

589 Koch, F.G., Johnson, A.M. and Pollard, D.D., 1981. Monoclinial bending of strata over
590 laccolithic intrusions. *Tectonophysics*, 74(3-4), pp.T21-T31.

591 Lu, H. and Fulthorpe, C.S., 2004. Controls on sequence stratigraphy of a middle Miocene-
592 Holocene, current-swept, passive margin: offshore Canterbury Basin, New
593 Zealand. *Geological Society of America Bulletin*, 116(11-12), pp.1345-1366.

594 Lu, H., Fulthorpe, C.S., Mann, P. and Kominz, M.A., 2005. Miocene-Recent tectonic and
595 climatic controls on sediment supply and sequence stratigraphy: Canterbury Basin, New
596 Zealand. *Basin Research*, 17(2), pp.311-328.

597 Magee, C., Briggs, F. and Jackson, C.A., 2013a. Lithological controls on igneous intrusion-
598 induced ground deformation. *Journal of the Geological Society*, 170(6), pp.853-856.

599 Magee, C., Hunt-Stewart, E. and Jackson, C.A.L., 2013b. Volcano growth mechanisms and
600 the role of sub-volcanic intrusions: Insights from 2D seismic reflection data. *Earth and*
601 *Planetary Science Letters*, 373, pp.41-53.

602 Magee, C., Maharaj, S.M., Wrona, T. and Jackson, C.A.L., 2015. Controls on the expression
603 of igneous intrusions in seismic reflection data. *Geosphere*, 11(4), pp.1024-1041.

604 Magee, C., Muirhead, J.D., Karvelas, A., Holford, S.P., Jackson, C.A., Bastow, I.D.,
605 Schofield, N., Stevenson, C.T., McLean, C., McCarthy, W. and Shtukert, O., 2016a. Lateral
606 magma flow in mafic sill complexes. *Geosphere*, 12(3), pp.809-841.

607 Magee, C., Duffy, O.B., Purnell, K., Bell, R.E., Jackson, C.A.L. and Reeve, M.T., 2016b.
608 Fault-controlled fluid flow inferred from hydrothermal vents imaged in 3D seismic reflection
609 data, offshore NW Australia. *Basin Research*, 28(3), pp.299-318.

610 Magee, C., Jackson, C.A.L., Hardman, J.P. and Reeve, M.T., 2017. Decoding sill
611 emplacement and forced fold growth in the Exmouth Sub-basin, offshore northwest
612 Australia: Implications for hydrocarbon exploration. *Interpretation*, 5(3), pp.SK11-SK22.

613 Milne, A.D., Simpson, C., Threadgold, P., 1975. Well completion report Resolution-1, for
614 BP, Shell, Todd (Canterbury) Services Limited. New Zealand Geological Survey
615 Unpublished open-file Petroleum Report PR648.

616 Montanari, D., Bonini, M., Corti, G., Agostini, A. and Del Ventisette, C., 2017. Forced
617 folding above shallow magma intrusions: Insights on supercritical fluid flow from analogue
618 modelling. *Journal of Volcanology and Geothermal Research*, 345, pp.67-80.

619 Morgan, S., Stanik, A., Horsman, E., Tikoff, B., de Saint Blanquat, M. and Habert, G., 2008.
620 Emplacement of multiple magma sheets and wall rock deformation: Trachyte Mesa intrusion,
621 Henry Mountains, Utah. *Journal of Structural Geology*, 30(4), pp.491-512.

622 Pagli, C., Wright, T.J., Ebinger, C.J., Yun, S.H., Cann, J.R., Barnie, T. and Ayele, A., 2012.
623 Shallow axial magma chamber at the slow-spreading Erta Ale Ridge. *Nature*
624 *Geoscience*, 5(4), p.284.

625 Planke, S., Rasmussen, T., Rey, S.S. and Myklebust, R., 2005, January. Seismic
626 characteristics and distribution of volcanic intrusions and hydrothermal vent complexes in the
627 Vøring and Møre basins. In *Geological Society, London, Petroleum Geology Conference*
628 *series* (Vol. 6, No. 1, pp. 833-844). Geological Society of London.

629 Pollard, D.D. and Johnson, A.M., 1973. Mechanics of growth of some laccolithic intrusions
630 in the Henry Mountains, Utah, II: bending and failure of overburden layers and sill
631 formation. *Tectonophysics*, 18(3-4), pp.311-354.

632 Polteau, S., Ferré, E.C., Planke, S., Neumann, E.R. and Chevallier, L., 2008. How are saucer-
633 shaped sills emplaced? Constraints from the Golden Valley Sill, South Africa. *Journal of*
634 *Geophysical Research: Solid Earth*, 113(B12).

635 Raymer, L.L., Hunt, E.R. and Gardner, J.S., 1980, January. An improved sonic transit time-
636 to-porosity transform. In *SPWLA 21st annual logging symposium*. Society of Petrophysicists
637 and Well-Log Analysts.

638 Reeves, J., Magee, C. and Jackson, C.L., 2018. Unravelling intrusion-induced forced fold
639 kinematics and ground deformation using 3D seismic reflection data. *Volcanica*, 1, 1-17.

640 Scheibert, J., Galland, O. and Hafver, A., 2017. Inelastic deformation during sill and laccolith
641 emplacement: Insights from an analytic elastoplastic model. *Journal of Geophysical*
642 *Research: Solid Earth*, 122(2), pp.923-945.

643 Schiøler, P., Raine, J.I., Crundwell, M>P., Griffin, A., Hollis, C.J. et al., 2011. Revised
644 biostratigraphy and well correlation, Canterbury Basin, New Zealand Ministry of Economic
645 Development New Zealand Unpublished Petroleum Report PR4365.

646 Schmiedel, T., Kjoberg, S., Planke, S., Magee, C., Galland, O., Schofield, N., Jackson,
647 C.A.L. and Jerram, D.A., 2017. Mechanisms of overburden deformation associated with the
648 emplacement of the Tulipan sill, mid-Norwegian margin. *Interpretation*, 5(3), pp.SK23-
649 SK38.

650 Schofield, N.J., Brown, D.J., Magee, C. and Stevenson, C.T., 2012. Sill morphology and
651 comparison of brittle and non-brittle emplacement mechanisms. *Journal of the Geological
652 Society*, 169(2), pp.127-141.

653 Schofield, N., Alsop, I., Warren, J., Underhill, J.R., Lehné, R., Beer, W. and Lukas, V., 2014.
654 Mobilizing salt: Magma-salt interactions. *Geology*, 42(7), pp.599-602.

655 Sclater, J.G. and Christie, P.A., 1980. Continental stretching: An explanation of the post-mid-
656 Cretaceous subsidence of the central North Sea basin. *Journal of Geophysical Research:
657 Solid Earth*, 85(B7), pp.3711-3739.

658 Sewell, R.J. and Gibson, I.L., 1988. Petrology and geochemistry of Tertiary volcanic rocks
659 from inland Central and South Canterbury, South Island, New Zealand. *New Zealand Journal
660 of Geology and Geophysics*, 31(4), pp.477-492.

661 Smallwood, J.R. and Maresh, J., 2002. The properties, morphology and distribution of
662 igneous sills: modelling, borehole data and 3D seismic from the Faroe-Shetland
663 area. *Geological Society, London, Special Publications*, 197(1), pp.271-306.

664 Spacapan, J.B., Galland, O., Leanza, H.A. and Planke, S., 2016. Igneous sill and finger
665 emplacement mechanism in shale-dominated formations: a field study at Cuesta del
666 Chihuido, Neuquén Basin, Argentina. *Journal of the Geological Society*, 174(3), pp.422-433.

667 Stearns, D.W., 1978. Faulting and forced folding in the Rocky Mountains foreland. *Laramide
668 folding associated with basement block faulting in the western United States: Geological
669 Society of America Memoir*, 151, pp.1-37.

670 Symonds, P.A., Planke, S., Frey, O. and Skogseid, J., 1998. Volcanic evolution of the
671 Western Australian continental margin and its implications for basin development. *The
672 Sedimentary Basins of Western Australia*, 2(1), pp.33-54.

673 Timm, C., Hoernle, K., Werner, R., Hauff, F., van den Bogaard, P., White, J., Mortimer, N.
674 and Garbe-Schönberg, D., 2010. Temporal and geochemical evolution of the Cenozoic
675 intraplate volcanism of Zealandia. *Earth-Science Reviews*, 98(1), pp.38-64.

676 Thomson, K. and Hutton, D., 2004. Geometry and growth of sill complexes: insights using
677 3D seismic from the North Rockall Trough. *Bulletin of Volcanology*, 66(4), pp.364-375.

678 Trude, J., Cartwright, J., Davies, R.J. and Smallwood, J., 2003. New technique for dating
679 igneous sills. *Geology*, 31(9), pp.813-816.

680 Uruski, C.I., 2010. New Zealand's deepwater frontier. *Marine and Petroleum Geology*, 27(9),
681 pp.2005-2026.

682 van Wyk de Vries, B., Márquez, A., Herrera, R., Bruña, J.G., Llanes, P. and Delcamp, A.,
683 2014. Craters of elevation revisited: forced-folds, bulging and uplift of volcanoes. *Bulletin of
684 Volcanology*, 76(11), p.875.

685 Wyllie, M.R.J., Gregory, A.R. and Gardner, L.W., 1956. Elastic wave velocities in
686 heterogeneous and porous media. *Geophysics*, 21(1), pp.41-70.

687

688 **9. Figure captions**

689 Figure 1: (A) Seismically imaged maximum forced fold amplitudes (F_{\max}) plotted against
690 maximum measured thicknesses (T_{\max}) of underlying sills or laccoliths from data within the:
691 (i) Bight Basin, offshore southern Australia (Jackson et al. 2013); (ii) Exmouth Sub-basin,
692 offshore north-western Australia (Magee et al. 2013a); and (iii) Rockall Basin, NE Atlantic
693 (Hansen & Cartwright, 2006). See Jackson et al. (2013) and Hansen & Cartwright (2006) for
694 information on error bars. (B) Field photograph showing folding of sandstone beds above the

695 Trachyte Mesa intrusion in the Henry Mountains, Utah, USA. (C) Sketch showing changes in
696 thickness of a massive red sandstone bed, shown in (B), over the Trachyte Mesa intrusion,
697 which corresponds to a reduction in porosity (after Morgan et al. 2008).
698

699 Figure 2: (A) Location of the Canterbury Basin within New Zealand. (B) Location of 2D
700 seismic lines and the Resolution-1 borehole used in this study.
701

702 Figure 3: Chronostratigraphic chart for the northern Canterbury Basin around Resolution-1,
703 highlighting different tectonic and igneous events (based on Carter, 1988; Fulthorpe et al.
704 1996; Killops et al. 1997; Timm et al. 2010; Uruski et al. 2010; Schiøler et al. 2011; Reeves
705 et al. 2018). Igneous events from Timm et al. (2010) correspond to: (i) = Geraldine and
706 Timaru Lavas; (ii) = Banks Peninsula; (iii) = Cookson Volcanics; (iv) = View Hill, Central
707 Canterbury. (1) = offshore sill emplacement events (Reeves et al. 2018). Fmn = Formation.
708

709 Figure 4: Spontaneous Potential (SP), Calliper (CAL), Gamma Ray (GR), and Sonic (ΔT)
710 logs from the Resolution-1 borehole plotted against depth. A plot of two-way time and
711 interval velocity changes with depth is also shown. The locations of the mapped horizons and
712 the Resolution Sill are highlighted.
713

714 Figure 5: (A and B) Interpreted, time-migrated seismic sections imaging the Resolution Sill
715 and neighbouring intrusions. Mapped stratigraphic horizons are marked and white-filled
716 arrows highlight onlap onto H6. Inset in (A) shows an uninterpreted, zoomed-in view of the
717 mounded structures. AI = acoustic impedance and VE = vertical exaggeration. See Figure 2B
718 for location of the seismic lines. Uninterpreted sections provided in Supplementary Figure 1.
719 (C) Depth-converted version of the seismic section shown in (B). Inset schematically shows
720 how erosion may modify the top of the fold and how F_{\max} and T_{\max} were measured.
721

722 Figure 6: (A and B) Depth-structure maps of top (TS) and base (BS) saucer-shaped sill
723 reflections interpolated from interpretation of the sill on the two seismic lines (thin white
724 lines) in Figure 5. The selected sill outline is constrained by the seismic reflection data and
725 assumes the sill likely has an elliptical shape, similar to sills observed elsewhere (see Hansen
726 et al. 2008). (C) Thickness map of TS–BS, i.e. where both horizons can be seismically
727 resolved, assuming a constant sill interval velocity of 5.02 km s^{-1} .
728

729 Figure 7: Plot of amplitude across the fold, at H3, measured directly from the seismic
730 reflection data (i.e. Figure 5C). We also show a range of sill thicknesses, for different seismic
731 interval velocities, across the intrusion where TS and BS can be distinguished; a sill thickness
732 profile considering a seismic interval velocity of 5.2 km s^{-1} is particularly highlighted because
733 this is the average interval velocity for the upper 50 m of the intrusion where it is intersected
734 by the Resolution-1 borehole. Thicknesses are not shown where the sill corresponds to a
735 tuned reflection package along the inclined limbs, but we do highlight the maximum (max.)
736 limit of separability and minimum (min.) limit of visibility for the sill. Note the lateral offset
737 of F_{\max} and T_{\max} .
738

739 Figure 8: (A and B) Depth-structure maps of horizons H6 and H3, highlighting the location of
740 the Resolution-1 borehole and intrusion-induced forced folds (black dashed lines) in the
741 vicinity. 2D seismic lines (white lines) also shown.
742

743 Figure 9: Plot of fold amplitude and sill thickness across the seismic line in Figure 5C,
744 highlighting how the measured fold shape and amplitude changes if the seismic data is
745 decompacted and backstripped.

Table 1. Resolution-1 continuous core petrology

Depth (m)	Rock type	Major phases*	Accessory phases*	Notes
1958.20	Quartz syenogabbro	Tau, Aeg, Plag, Ano, Ilm	Qtz, Bio, Apa, Chl	Tau is granular and sub-ophitic; Tau rimmed by Aeg; Ano rims Plag
1958.50	Olivine teschenite	Tau, Ol, Plag, Ana	Horn, Mag, Apa, Chl, Ilm, Ano	Ano occasionally rims Plag; Tau is ophitic and encloses Ol and Plag
1958.90	Teschenite	Tau, Plag, Ana, Ano	Apa, Ilm, Bio, Ol	Tau forms large ophitic crystals; Ano rims Plag
1959.20	Olivine teschenite	Tau, Ol, Plag, Ana	Horn, Mag, Apa, Chl, Ilm, Ano	Ano occasionally rims Plag; Tau is ophitic and encloses Ol and Plag
1959.30	Leucoteschenite	Plag, Ano, Ana	Apa, Ilm, Tau	Ano rims Plag; very little Tau
1959.45	Teschenite	Tau, Plag, Ana, Ano	Apa, Ilm, Bio, Ol	Tau forms large ophitic crystals; Ano rims Plag
1959.75	Leucoteschenite	Plag, Ano, Ana	Apa, Ilm, Tau	Ano rims Plag; very little Tau
1960.30	Teschenite	Tau, Plag, Ana, Ano	Apa, Ilm, Bio, Ol	Tau forms large ophitic crystals; Ano rims Plag
1960.60	Leucoteschenite	Plag, Ano, Ana	Apa, Ilm, Tau	Ano rims Plag; very little Tau
1962.30	Teschenite	Tau, Plag, Ana, Ano	Apa, Ilm, Bio, Ol Tau, Horn, Mag, Apa, Chl, Ilm, Ano	Tau forms large ophitic crystals; Ano rims Plag
1962.50	Olivine leucoteschenite	Ol, Plag, Ana		Ano occasionally rims Plag
1962.80	Olivine teschenite	Tau, Ol, Plag, Ana	Horn, Mag, Apa, Chl, Ilm, Ano Tau, Horn, Mag, Apa, Chl, Ilm, Ano	Ano occasionally rims Plag; Tau is ophitic and encloses Ol and Plag
1963.05	Olivine leucoteschenite	Ol, Plag, Ana		Ano occasionally rims Plag

*Tau = Titanaugite; Aeg = Aegerine augite; Plag = Plagioclase; Ano = Anorthoclase; Ol = Olivine; Ana = Analcite; Ilm = Ilmenite; Qtz = Quartz; Apa = Apatite; Chl = Chlorite; Horn = Ti-hornblende; Mag = Magnetite; Bio = Biotite

Figure 1

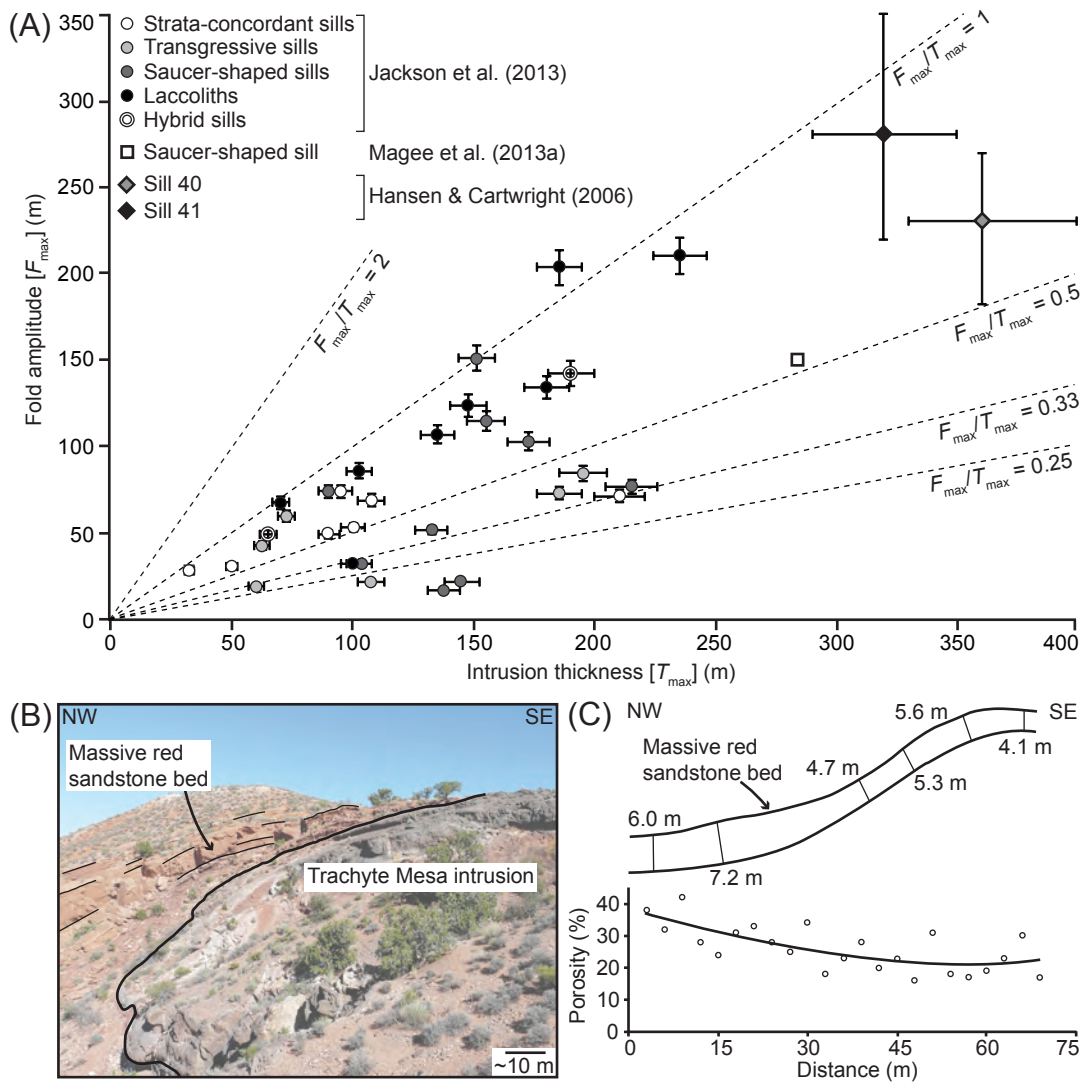


Figure 2

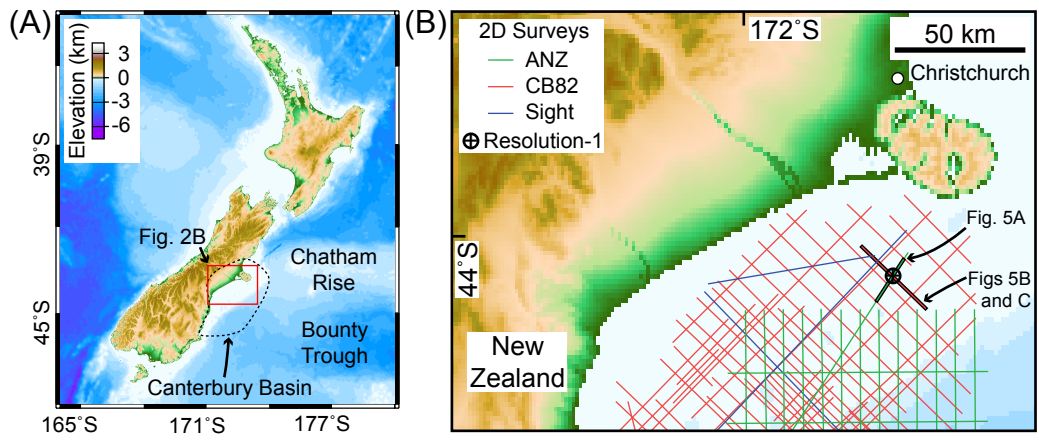


Figure 3

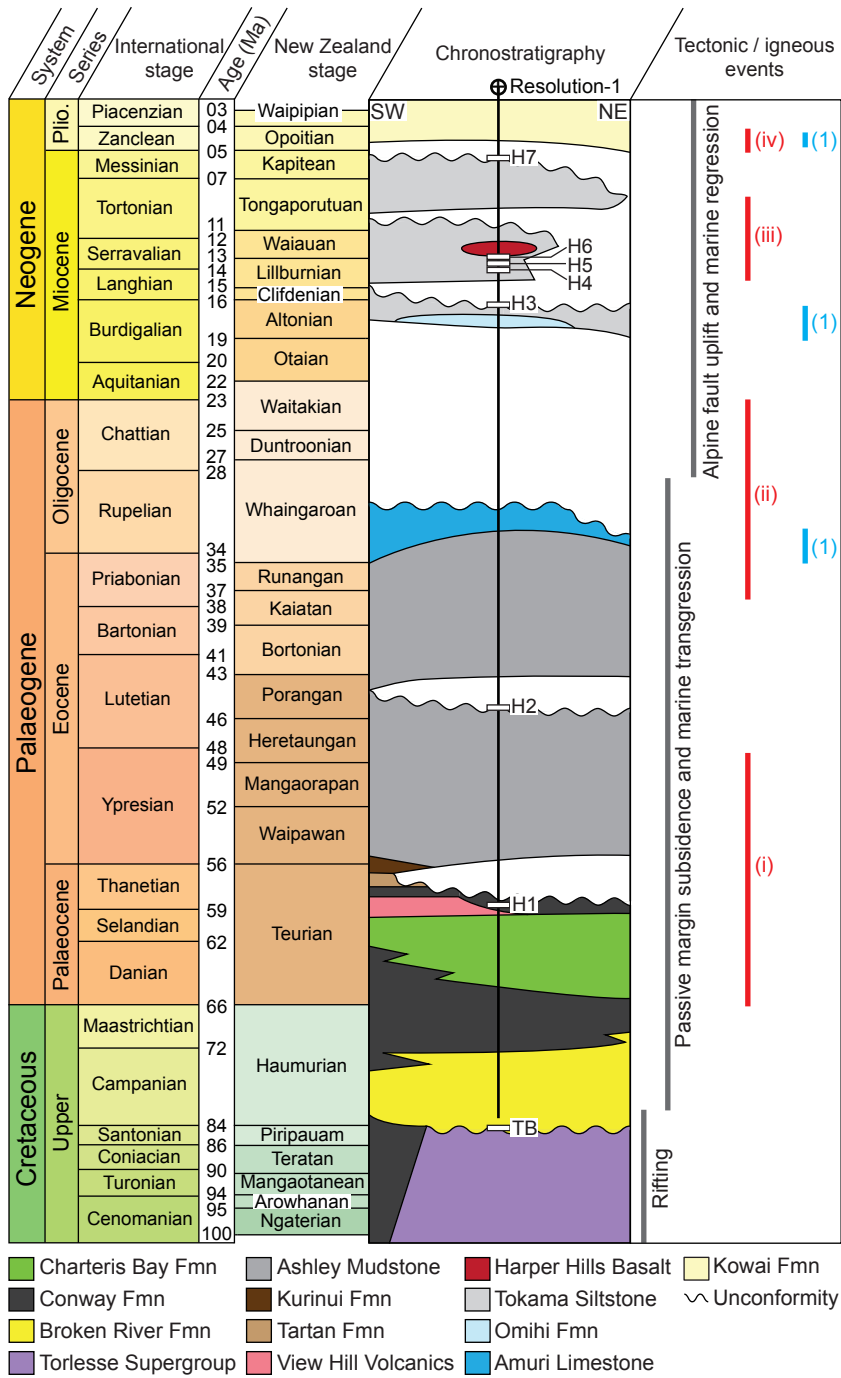


Figure 4

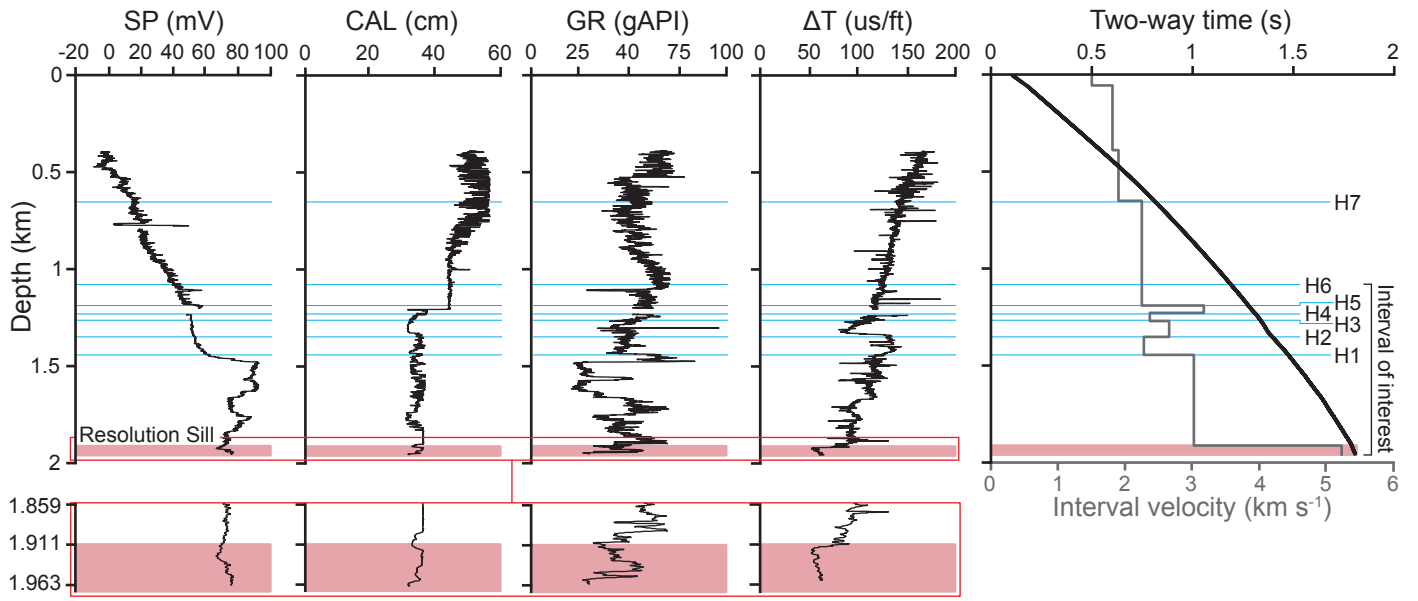


Figure 5

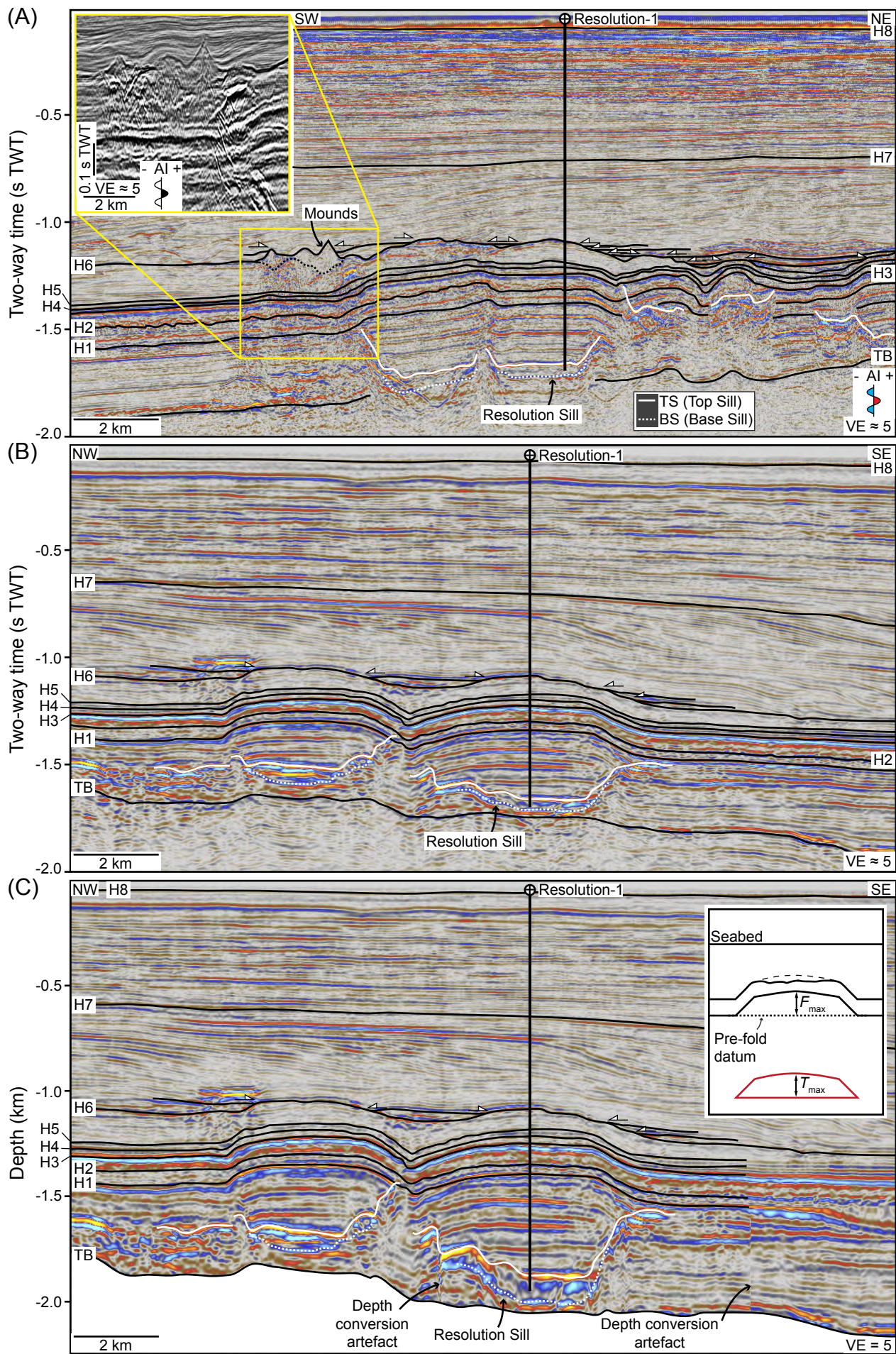


Figure 6

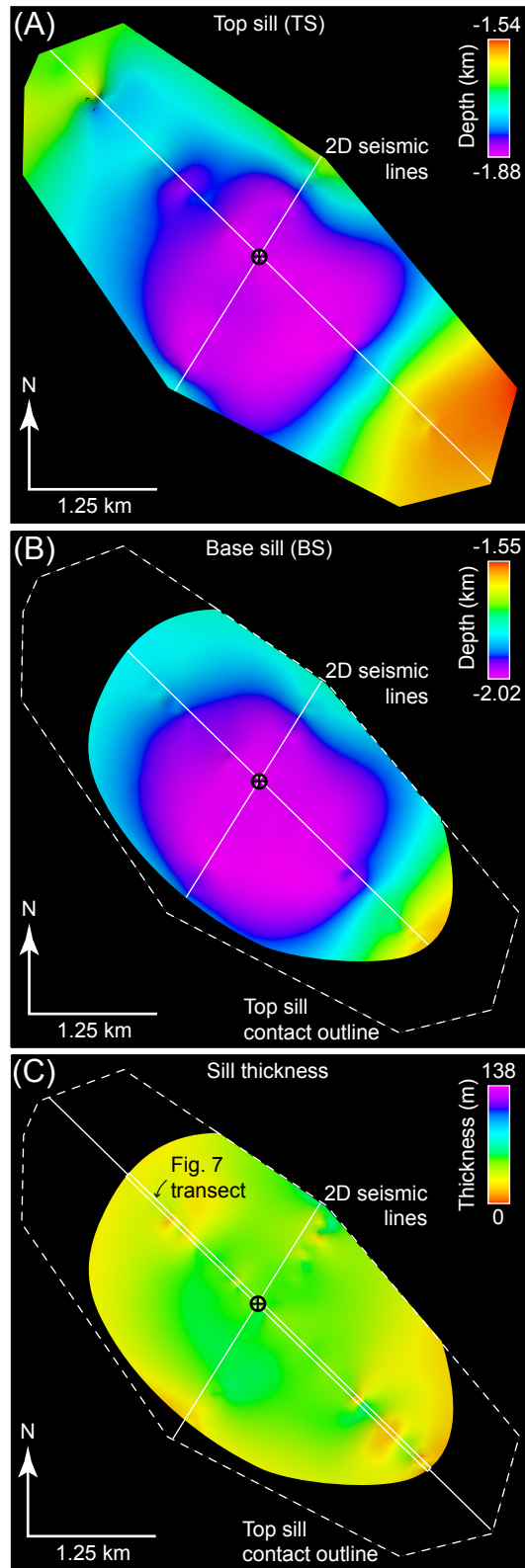


Figure 7

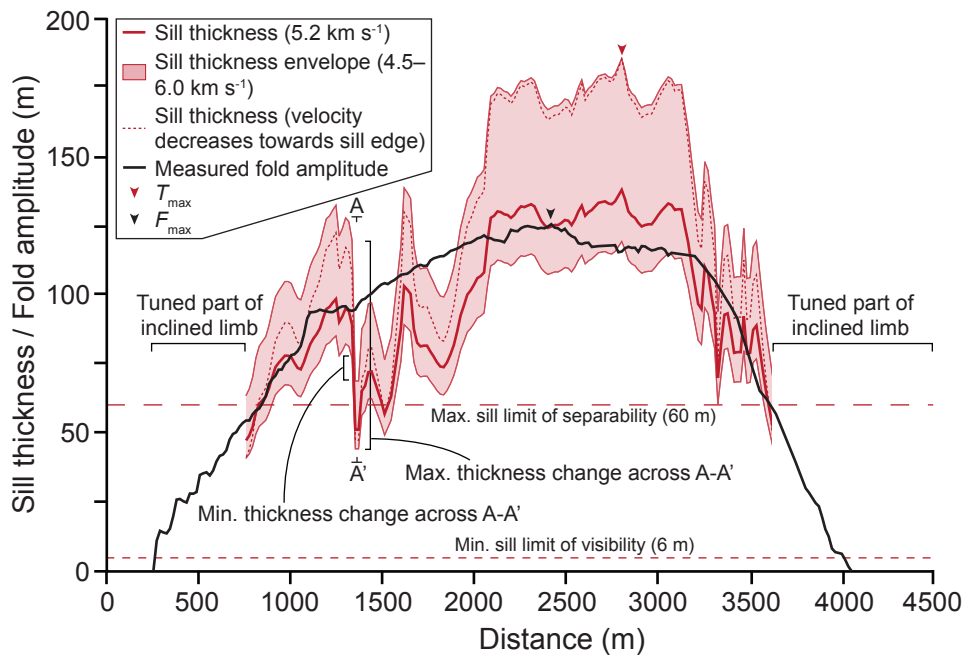


Figure 8

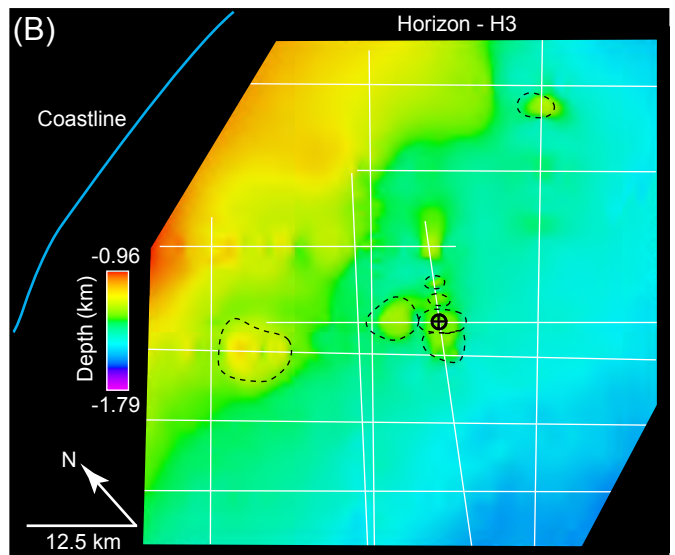
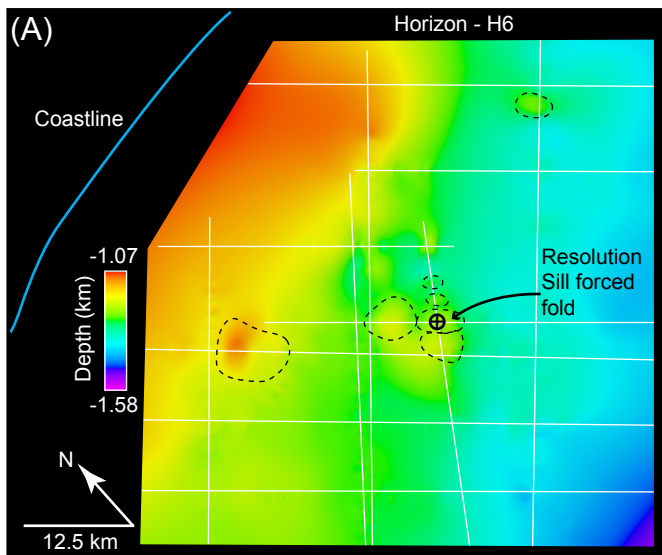


Figure 9

